A Methodology for Obtaining Super-Resolution Images and Depth Maps from RGB-D Data

Daniel B. Mesquita, Mario F. M. Campos, Erickson R. Nascimento
Computer Science Department
Universidade Federal de Minas Gerais
Belo Horizonte, MG, Brazil
E-mail: {balbino,mario,erickson}@dcc.ufmg.br

***Abstract*—The emergence of low cost sensors capable of providing texture and depth information of a scene is enabling the deployment of several applications such as gesture and object recognition and three-dimensional reconstruction of environments. However, commercially available sensors output low resolution data, which may not be suitable when more detailed information is necessary. With the purpose of increasing data resolution, at the same time reducing noise and filling the holes in the depth maps, in this work we propose a method that combines depth fusion and image reconstruction in a super-resolution framework. By joining low-resolution intensity images and depth maps in an optimization process, our methodology creates new images and depth maps of higher resolution and, at the same time, minimizes issues related with the absence of information (holes) in the depth map. Our experiments show that the proposed approach has increased the resolution of the images and depth maps without significant spawning of artifacts. Considering three different evaluation metrics, our methodology outperformed other three techniques commonly used to increase the resolution of combined images and depth maps acquired with low resolution, commercially available sensors.**

***Keywords*-Super-resolution, convex optimization, RGB-D data, 3D reconstruction, computer vision.**

I. Introduction

The increasing availability of low-cost sensors capable of capturing both image and depth information, also known as RGB-D sensors such as Kinect, opened a wide research horizon for several methodologies involving processing of geometry and visual data. If on one hand these sensors can provide a good initial estimate of the three-dimensional structure of the scene with texture embedded, on the other hand such sensors provide low resolution images and noisy depth maps. Since the results of several algorithms are directly dependent on the quality and amount of detail present in the data, sharpening images and depth maps can increase the accuracies for object recognition and improve precision of 3D alignment and reconstruction [1].

In general, a super-resolution method can be divided into two main steps: registration and interpolation. The first step consists of finding the transformation of the frames to the same coordinate system (*e.g.* the coordinate system defined by camera's pose in the acquisition of the first image in the sequence). The second step estimates the intensity information of pixels for a larger grid.

(a) Low Resolution Point Cloud (b) Super-Resolution Point Cloud

Figure 1. An example of the reconstruction provided by our methodology. The left image shows a point cloud of the original image from the Freiburg dataset [2] and the right image the corresponding point cloud estimated by our algorithm. It can be seen that our method increase the point cloud resolution (e.g. keyboard and milk box) as well as reconstruct the lost and deteriorated regions of the cloud (e.g. monitor). The background are shown in blue.

When the sensor moves freely in the scene, matching between pixels is usually performed by optical flow. However, this approach has high computational cost and cannot be applied when sensor displacements are large. Therefore, several techniques have been proposed to use depth information in order to estimate pixel correspondences making the estimation more efficient. Despite the quality provided by these techniques, it is necessary to provide the depth information and in most cases, image reconstruction methods are used to estimate the depth. Although these strategies are able to determine the correspondence, they use a depth map which is a rough approximation of the real map. This limits the image quality estimation, since such depth maps contain errors that are propagated to the interpolation step.

The main contribution of this work[1] is a new method for 3D reconstruction based on an optimization approach which provides super-resolution intensity and depth images acquired by a low resolution sensor, such as commercially available RGB-D sensors. Our proposed model is defined as a convex optimization problem for which state of the art optimization techniques are employed to find the best solution. Figure 1 shows a high resolution point cloud estimated by our method applied in a sequence extracted from Freiburg dataset [2].

II. Related Works

In general, the methodologies for super-resolution may be broadly divided into two main categories: Super-resolution

[1]This work relates to a Master dissertation.

by example and reconstruction based super-resolution. While methodologies in the former category use learning-based approaches in order to increase the resolution of images, in the latter it is assumed as a basic premise that the low resolution images (LR) are subsamples with subpixel precision of some high resolution image (HR), and which can be used to reconstruct the original HR image.

Thanks to the increasing access to devices capable of obtaining geometrical data from the scene, several super-resolution techniques have included the use of depth maps in their approach. In [3] the authors proposed a method based on MRF (Markov Random Fields) to integrate the depth information acquired by a laser scanner with images from a high resolution camera. A similar technique is presented in [4]. By using a ToF (Time-of-flight) camera to acquire range images and applying a bilateral filter, they present an iterative algorithm to enlarge the spatial resolution of depth maps.

In [5], the problem of super-resolution is modeled by using a calibrated three-dimensional scene and a probabilistic framework based on MAP-MRF. Although their method efficiently handles occlusions in the depth maps, the algorithm does not estimate depth, which reduces the quality of their results in regions which contain holes in the depth map. In [6], the authors present a method for increasing the precision of the reconstruction from 3D video using multiple static cameras and a formulation based on MRF and graph-cuts.

In [7] the authors used an energy functional that simultaneously estimates the texture and the 3D object surface. The limitation of that work is that the displacement of the camera and the correspondence between images must be known *a priori*.

Unlike [7], which applied an energy functional to simultaneously estimate the texture and geometry in higher resolution, [8] uses a formulation composed of an iterative technique based on graph-cuts and an Expectation Maximization (EM) procedure. The main drawback of their methodologies is the high computational cost required to create the HR images and depth maps.

Several approaches have modeled the reconstruction problem in super-resolution as a convex optimization problem, and the most popular are based on variational methods. In general, these methods use a primal-dual algorithm to solve the optimization problem. In [9], a first order primal-dual algorithm is applied to estimate super-resolution images. Although, the authors show the robustness of their method for different types of noise and different scale factors, the results degenerate in the presence of Gaussian noise.

A recent work related to ours is presented in [10]. Similar to our technique, the authors propose a methodology which uses a first-order primal-dual algorithm to perform three-dimensional reconstruction and obtains super-resolution data simultaneously, using as input a set of images from different views. In spite of the good results achieved for images, the reconstructed depth map does not take into account the depth information, and it is highly sensitive to image noise typically present in low cost RGB-D sensors. In order to overcome such limitations, our approach solves the optimization problem considering both visual and geometrical data.

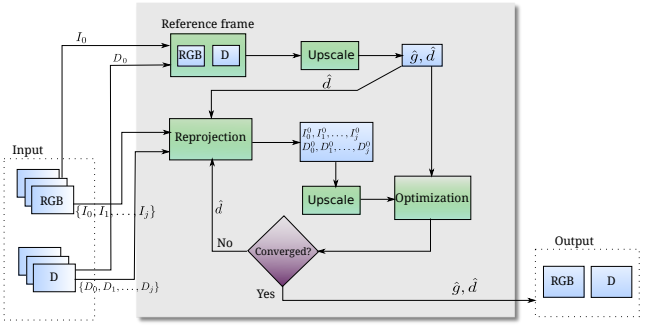

Figure 2. The main steps of the super-resolution methodology. First, all LR RGB-D images are reprojected to the reference frame and then an estimation of the super-resolution image $\boldsymbol{g}$ and depth $\boldsymbol{d}$ with the best reconstruction of the data is obtained in an iterative process.

III. Methodology

In this section we detail the design of our methodology. The input is a set of LR images $\boldsymbol{I}_j$ and depth maps $\boldsymbol{D}_j$ with size $M \times N$ and their corresponding camera poses $\boldsymbol{P}_j \in \mathbb{SE}(3)$ in which $0 \leq j \leq J$. The output is an image $\boldsymbol{g}$ and a depth map $\boldsymbol{d}$ both with $sM \times sN$ size, $s \in \mathbb{R}$ is the scale factor. Both are estimated w.r.t. the pose of the reference image $\boldsymbol{P}_0$.

Our method is composed of three main steps: i) First, an initial estimation for $\boldsymbol{g}$ and $\boldsymbol{d}$ is computed by upscaling $\boldsymbol{D}_0$ and $\boldsymbol{I}_0$; ii) Then the input images and depth maps are reprojected onto the reference frame by using the depth information from $\boldsymbol{d}$; iii) Finally, the optimization process computes a new estimation for $\boldsymbol{g}$ and $\boldsymbol{d}$. These three steps are repeated until a convergence criteria is satisfied. The diagram in Figure 2 depicts these steps and the data flow from the LR images and depth maps to the final HR images and depth maps.

A. Modeling

Our methodology computes the super-resolution images and depth maps by modeling the problem as a convex optimization problem. The model adopted is based on three main parts:

- Image super-resolution – Establishes the relationship between a super-resolution image $\boldsymbol{g}$ and multiple input LR images $\boldsymbol{I}_i, 0 \leq j \leq J$.
- Depth super-resolution – Defines the relationship between a depth map in super-resolution $\boldsymbol{d}$ and multiple input depths $\boldsymbol{D}_i, 0 \leq j \leq J$.
- Regularization – Maintains consistency of the final solution avoiding degenerate results.

B. Super-Resolution from Images

The relationship between the reference frame and the super-resolution image is given by:

$$\boldsymbol{I}_0 = \boldsymbol{S} * \boldsymbol{B} * \boldsymbol{g}, \tag{1}$$

where $\boldsymbol{B}$ is a blurring Gaussian kernel with standard deviation s and a support size $(s-1)^{(1/2)}$ and $\boldsymbol{S}$ is the downsampling operator.

Assuming photometric consistency, the pixel with coordinates $\boldsymbol{x} = [x, y]^T$ in image $\boldsymbol{I}_0$ and depth $\boldsymbol{D}_0(\boldsymbol{x})$ has its corresponding coordinates in image $\boldsymbol{I}_j$ ($\forall j \in \{0, \ldots, J\}$) given by:

$$\boldsymbol{I}_0(\boldsymbol{x}) = \boldsymbol{I}_j(f(\boldsymbol{x}, \boldsymbol{D}_0(\boldsymbol{x}))), \tag{2}$$

where $f(\boldsymbol{x}, \boldsymbol{D}_0(\boldsymbol{x})) : R^2 \times R \rightarrow R^2$ is the function which maps the pixel $\boldsymbol{x}$ with depth $\boldsymbol{D}_0(\boldsymbol{x})$ from the reference image to $\boldsymbol{I}_j$. This mapping function will be presented in more detail in section III-E.

Thus, the problem of computing a super-resolution image consists of estimating an image $\boldsymbol{g}$ that minimizes the error between all low-resolution images:

$$\arg\min_{\boldsymbol{g}} \int_{\Omega} \sum_{j=0}^{J} \|(\boldsymbol{S} * \boldsymbol{B} * \boldsymbol{g})(\boldsymbol{x}) - \boldsymbol{I}_j(f(\boldsymbol{x}, \boldsymbol{D}_0(\boldsymbol{x}))\| d\boldsymbol{x}, \tag{3}$$

where Ω is the image domain.

C. Super-resolution of the Depth Maps

We also want to find a super-resolution depth map $\boldsymbol{d}$. Similarly to the image enlargement, we minimize the error between all the reprojected LR depth maps:

$$E_D = \arg\min_{d} \sum_{j=0}^{J} \|\upsilon_j(\boldsymbol{d})\|_1 \tag{4}$$

$$= \arg\min_{d} \sum_{j=0}^{J} \|\boldsymbol{S} * \boldsymbol{B} * \boldsymbol{d} - \boldsymbol{D}_j^0\|, \tag{5}$$

where $\boldsymbol{D}_j^0$ is the depth map $\boldsymbol{D}_j$ reprojected to the reference frame.

D. Regularization

The regularization term is used to keep the consistency of the final solution, and in this work we use the Huber norm [11] for the intensity image $\boldsymbol{g}$ and depth $\boldsymbol{d}$. In addition to preserving discontinuities in the final solution, the Huber norm also prevents degenerate solutions.

The norm for $\boldsymbol{g}$ is defined by the following function:

$$\|\nabla g\|_{\alpha_g}(x, y) = \begin{cases} \frac{|\nabla g|^2}{2\alpha_g} & \text{if} |\nabla g| \leq \alpha_g, \\ |\nabla g| - \frac{\alpha_g}{2} & \text{if} |\nabla g| > \alpha_g, \end{cases} \tag{6}$$

where ∇ is the linear operator corresponding to the image gradient. The Huber norm $\|d\|_{\alpha_d}$ is calculated in the same way.

E. Reprojection Function

The reprojection function that maps a pixel $\boldsymbol{x} = [x, y]^T$ with depth $\boldsymbol{d}(\boldsymbol{x})$ in the reference frame to $\boldsymbol{I}_j$ is defined as:

$$f(\boldsymbol{x}, \boldsymbol{d}(\boldsymbol{x})) = h(\boldsymbol{K}\boldsymbol{P}_{j,0}\boldsymbol{d}(\boldsymbol{x})\boldsymbol{K}^{-1}[x, y, 1]^T), \tag{7}$$

where $\boldsymbol{K}$ is the projection matrix and h is the dehomogenization function (Figure 3).

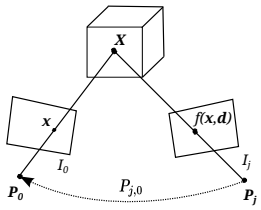

Figure 3. The reprojection function $f(\boldsymbol{x}, \boldsymbol{d})$ establishes the correspondence between the pixels in $\boldsymbol{I}_0$ and $\boldsymbol{I}_j$ based on the depth information at the reference frame.

By using the reprojection function, the image $\boldsymbol{I}_j(f(\boldsymbol{x}, \boldsymbol{d}(\boldsymbol{x})))$ which has the corresponding pixels of the reference image $\boldsymbol{I}_0(\boldsymbol{x})$ is given by:

$$\boldsymbol{I}_j(f(\boldsymbol{x}, \boldsymbol{d}(\boldsymbol{x}))) = \boldsymbol{I}_j(h(\boldsymbol{K}\boldsymbol{P}_{j,0}\boldsymbol{d}(\boldsymbol{x})\boldsymbol{K}^{-1}[x, y, 1]^T)). \tag{8}$$

To simplify the notation without using pixel reference, we define the reprojection operator $W(\boldsymbol{I}_j, \boldsymbol{d})$ which warps the image $\boldsymbol{I}_j$ to the reference frame in the form:

$$W(\boldsymbol{I}_j, \boldsymbol{d}) = \boldsymbol{I}_j(f(\boldsymbol{x}, \boldsymbol{d}(\boldsymbol{x})))d\boldsymbol{x}, \qquad \forall x \in \Omega. \tag{9}$$

F. Image super-resolution and reconstruction

Although the RGB-D sensor provides an initial estimation of the depth map $\boldsymbol{D}_0$ of the scene, such data is noisy and often there is no depth information in some areas (due to sensor limitations) producing holes in the depth map. To overcome this issue we use a similar approach to the works of [12], [10] in which we estimate $\boldsymbol{d}$ iteratively and simultaneously to $\boldsymbol{g}$.

Considering the first-order Taylor expansion of $W(\boldsymbol{I}_j, \boldsymbol{d})$ we approximate a change in the image $W(\boldsymbol{I}_j, \boldsymbol{d})$ w.r.t. a small change of depth at an initial value $\boldsymbol{d_0}$ as:

$$W(\boldsymbol{I}_j, \boldsymbol{d}) \simeq W(\boldsymbol{I}_j, \boldsymbol{d}_0) + \frac{\delta}{\delta d} W(\boldsymbol{I}_j, \boldsymbol{d})\Big|_{\boldsymbol{d}=\boldsymbol{d_0}} \cdot (\boldsymbol{d} - \boldsymbol{d_0}). \tag{10}$$

Therefore, the objective function described by Equation 3 can be linearized as:

$$\arg\min_{g,d} \sum_{j=0}^{J} \|\boldsymbol{S} * \boldsymbol{B} * \boldsymbol{g} - \{W(\boldsymbol{I}_j, \boldsymbol{d}_0) + \boldsymbol{u_j} \cdot (\boldsymbol{d} - \boldsymbol{d_0})\}\|_1, \tag{11}$$

where $\boldsymbol{u_j}$ is the simplified notation for $\frac{\delta}{\delta d} W(\boldsymbol{I}_j, \boldsymbol{d})\big|_{d_0}$, which can be calculated by applying the chain rule:

$$\boldsymbol{u_j} = \frac{\delta}{\delta d} W(\boldsymbol{I}_j, \boldsymbol{d}) = \nabla I_j(f(\boldsymbol{x}, \boldsymbol{d}(\boldsymbol{x}))) \cdot \frac{\delta f(\boldsymbol{x}, \boldsymbol{d}(\boldsymbol{x}))}{\delta d}. \tag{12}$$

In our solution, instead of applying the downsampling operator $\boldsymbol{S}$ to the image $\boldsymbol{g}$ at each iteration, we upscale the input images to the size $sM \times sN$ using bicubic interpolation.

Therefore, the function corresponding to the image term is

given by:

$$E_I = \arg\min_{g,d} \sum_{j=0}^{J} \|\rho_j(\boldsymbol{g}, \boldsymbol{d})\| \tag{13}$$

$$= \arg\min_{g,d} \sum_{j=0}^{J} \|\boldsymbol{B} * \boldsymbol{g} - \{W(\hat{\boldsymbol{I}}_j, \boldsymbol{d_0}) + \hat{\boldsymbol{u}}_{\boldsymbol{d}}.(\boldsymbol{d} - \boldsymbol{d_0})\}\|_1, \tag{14}$$

the operator $\hat{\cdot}$ represents the upscaled version of the image.

G. Final Cost Function

The energy function used in this work takes into account the cost functions E_I and E_D that correspond to merging multiple images and multiple depth maps respectively and the regularization term E_R.

The parameters λ_I and λ_D control the degree of regularization of the energy functional $E(\boldsymbol{g}, \boldsymbol{d})$ as follows:

$$E(\boldsymbol{g}, \boldsymbol{d}) = \|\nabla \boldsymbol{g}\|_{\alpha_{\boldsymbol{g}}} + \|\nabla \boldsymbol{d}\|_{\alpha_{\boldsymbol{d}}} + \lambda_I \sum_{j=0}^{J} \|\rho_j(\boldsymbol{g}, \boldsymbol{d})\|_1 + \lambda_D \sum_{j=0}^{J} \|\upsilon_j(\boldsymbol{d})\|_1. \tag{15}$$

The influence of the regularization term is bigger for small values of λ_I and λ_D. This creates a smoothing effect on the final result. In this work we have used $\lambda_I = 0.5$ and $\lambda_D = 0.3$.

H. Solution by Primal-Dual method

In this section we present a solution for Equation 15 based on the first order primal dual algorithm of [13]. Let Equation 15 be a min-max saddle point problem with a primal-dual formulation using Fenchel duality. For simplicity, only one adjacent frame will be used, then Equation 15 can be rewritten as:

$$E(\boldsymbol{g}, \boldsymbol{d}) = \|\nabla \boldsymbol{g}\|_{\alpha_g} + \|\nabla \boldsymbol{d}\|_{\alpha_d} + \lambda_I \|\rho_j(\boldsymbol{g}, \boldsymbol{d})\|_1 + \lambda_D \|\upsilon(\boldsymbol{d})\|_1. \tag{16}$$

Considering the dual variables $\mathbf{p}, \mathbf{q}, \mathbf{r}, \mathbf{s}$ for each term of Equation 16, the primal dual formulation can be defined by:

$$\min_{\boldsymbol{g},\boldsymbol{d}} \max_{\boldsymbol{p},\boldsymbol{q},\boldsymbol{r},\boldsymbol{s}} \langle \nabla \boldsymbol{g}, \boldsymbol{p} \rangle + \langle \nabla \boldsymbol{d}, \boldsymbol{q} \rangle + \lambda_I \langle \rho_j(\boldsymbol{g}, \boldsymbol{d}), \boldsymbol{r} \rangle + \lambda_D \ \langle \upsilon_j(\boldsymbol{d}), \boldsymbol{s} \rangle + \frac{\alpha_g}{2} \|\boldsymbol{p}\|_2^2 + \frac{\alpha_d}{2} \|\boldsymbol{q}\|_2^2 + F^*(\boldsymbol{p}) + F^*(\boldsymbol{q}) + F^*(\boldsymbol{r}) + F^*(\boldsymbol{s}), \tag{17}$$

where $F^*(\boldsymbol{p})$ is the dual function of the L^1 norm and is expressed as:

$$F^*(\boldsymbol{p}) = \begin{cases} 0 & \text{if } \|\boldsymbol{p}\| \leq 1 \\ \infty & \text{otherwise.} \end{cases} \tag{18}$$

This formulation expresses the same optimization problem, but with a function which is differentiable at all points.

The method used to solve the optimization problem defined by Equation 17 is an iterative algorithm, which has the steps determined by:

$$\begin{aligned}
\boldsymbol{p}^{n+1} &= \prod\nolimits_{\|\boldsymbol{p}\|_\infty \leq 1} \left\{ \frac{\boldsymbol{p}^n + \sigma \nabla \bar{\boldsymbol{g}}^n}{1 + \sigma \alpha_g} \right\}, \\
\boldsymbol{q}^{n+1} &= \prod\nolimits_{\|\boldsymbol{q}\|_\infty \leq 1} \left\{ \frac{\boldsymbol{q}^n + \sigma \nabla \bar{\boldsymbol{d}}^n}{1 + \sigma \alpha_d} \right\}, \\
\boldsymbol{r}^{n+1} &= \prod\nolimits_{\|\boldsymbol{r}\|_\infty \leq 1} \{\boldsymbol{r}^n + \sigma \rho(\bar{\boldsymbol{g}}^n, \bar{\boldsymbol{d}}^n)\}, \\
\boldsymbol{s}^{n+1} &= \prod\nolimits_{\|\boldsymbol{s}\|_\infty \leq 1} \{\boldsymbol{s}^n + \sigma \upsilon(\bar{\boldsymbol{d}}^n)\}, \\
\boldsymbol{g}^{n+1} &= \boldsymbol{g}^n + \tau \left(div \boldsymbol{p}^{n+1} - \lambda_I \boldsymbol{B}^T \boldsymbol{r}^{n+1} \right), \\
\boldsymbol{d}^{n+1} &= \boldsymbol{d}^n + \tau \left(div \boldsymbol{q}^{n+1} - \lambda_I \hat{\boldsymbol{u}}_{\boldsymbol{d}} \boldsymbol{r}^{n+1} - \lambda_D \boldsymbol{B}^T \boldsymbol{s}^{n+1} \right), \\
\bar{\boldsymbol{g}}^{n+1} &= 2\boldsymbol{g}^{n+1} - \boldsymbol{g}^n, \\
\bar{\boldsymbol{d}}^{n+1} &= 2\boldsymbol{d}^{n+1} - \boldsymbol{d}^n,
\end{aligned} \tag{19}$$

where div is the divergence operator and $\prod_{\|\boldsymbol{p}\|_\infty \leq 1}(\cdot)$ refers to the proximal operator of the dual variables and are subject to the restrictions described in Equation 17 and consists of a simple projection on the unit circle by the following formula:

$$p = \prod_{\|p\|_\infty \leq 1} (\bar{p}) \Leftrightarrow p_{ij} = \frac{\bar{p_{ij}}}{\max\{1, |\bar{p_{ij}}|\}}. \tag{20}$$

The extension for multiple images involves creating dual variables $\boldsymbol{r_i}$ and $\boldsymbol{s_i}$ for each image and update the solution in the form:

$$\boldsymbol{r}_{\boldsymbol{j}}^{n+1} = \prod\nolimits_{\|\boldsymbol{r_j}\|_\infty \leq 1} \{\boldsymbol{r}_{\boldsymbol{j}}^n + \sigma \rho_j(\bar{\boldsymbol{g}}^n, \bar{\boldsymbol{d}}^n)\}, \tag{21}$$

$$\boldsymbol{s}_{\boldsymbol{j}}^{n+1} = \prod\nolimits_{\|\boldsymbol{s_j}\|_\infty \leq 1} \{\boldsymbol{s}_{\boldsymbol{j}}^n + \sigma \upsilon_j(\bar{\boldsymbol{d}}^n)\}, \tag{22}$$

$$\boldsymbol{g}^{n+1} = \boldsymbol{g}^n + \tau div \boldsymbol{p}^{n+1} - \tau \lambda_I \boldsymbol{B}^T \sum_{j=0}^{J} \boldsymbol{r}_{\boldsymbol{j}}^{n+1}, \tag{23}$$

$$\boldsymbol{d}^{n+1} = \boldsymbol{d}^n + \tau div \boldsymbol{q}^{n+1} - \tau \lambda_I \sum_{j=0}^{J} \hat{\boldsymbol{u}}_{\boldsymbol{j}} \boldsymbol{r}_{\boldsymbol{j}}^{n+1} - \tau \lambda_D \boldsymbol{B}^T \sum_{j=0}^{J} \boldsymbol{s}_{\boldsymbol{j}}^{n+1}. \tag{24}$$

The timesteps σ and τ control the rate of convergence and we choose values according to [13]. Since the reconstruction term in Equations 21 and 24 define a solution space which may not be uniformly convex on all dimensions, we applied a pre-preconditioning process as discussed in [14].

I. Multi-scale Super-resolution approach

The linearization described in Equation 11 is valid only for small displacements. Moreover, the problem of image reconstruction is non-linear and may converge to local minimum. In order tackle with this issues we use a multi-scale coarse-to-fine approach. By using a set of scales $\{s_0, s_1, \ldots, s\}$ in ascending order, we estimate the depth map $\boldsymbol{d}$ and use it as input depth $\boldsymbol{d_0}$ on the next scale in the sequence.

IV. Experiments

We performed several experiments to evaluate our methodology both quantitatively and qualitatively. Synthetic images and real images were used for qualitative analysis. We also compare our results against the works of [10] and [9], which will be denoted as SSRDI and SR respectively. To simplify the nomenclature, we named our method as RGBD-SR.

A. Synthetic Images

All synthetic images were created based on the "Venus" sequence from the Middlebury dataset [15]. The "Venus" sequence is composed of an intensity image and a depth map of size 434×383 pixels. With the purpose of simulating holes, which is very common in RGB-D low cost sensors (such as Kinect, for example), we included a hole with dimensions 260×20 in the center of the depth map by setting all values to zero.

In the first experiment, we generated a set with 14 LR images by applying small displacements (rotation and translation transforms). We also included a synthetic hole in 7 images, and downscaled the images to 108×95 pixels. The images were used as input for the super-resolution algorithm in order to restore to its original size, which allow us to evaluate the result of the enlargement. For all tests the virtual camera positions are known and given as input in the optimization process.

For the quantitative analysis we generated 11 image sets, each one composed of 7 images and 7 depth maps. We included holes in all depth maps and a virtual camera was placed at arbitrary positions. We used different distances between the virtual camera and the reference frame for each set of images. By increasing this distance we are able to evaluate the robustness of the algorithm for large displacements. We evaluate the resulting HR images and depth maps by comparing then to the original. As quality assessment metric we use MSSIM (Mean Structural Similarity Index) and PSNR (Peak signal-to-noise ratio) for the images and MSSIM and RMSE (Root Mean Squared Error) for the depth maps.

Figure 4 shows the results for each set of different distances. One can see that our method presents better results both for the MSSIM and PSNR (considering the results in the images). The blue curve remains consistently above the other curves independent of increasing the distance. Figures 4c and 4d show the results for depth maps. Our method outperforms the others for both metrics.

B. Results on a real dataset

To perform a quantitative analysis with the proposed method in a real environment, we used the Kinect sensor to capture intensity images with resolution of 640×480 and $1,280 \times 960$. The latter were used as groundtruth. After acquiring 10 images and its respective depth maps with the default 640×480 Kinect resolution (Figure 6), we ran the methodologies to compute such images in resolution of $1,280 \times 960$, then compared this result with the groudtruth image with quality assessment metrics. Every input frame is captured with small displacements w.r.t. the reference frame, in which we use the

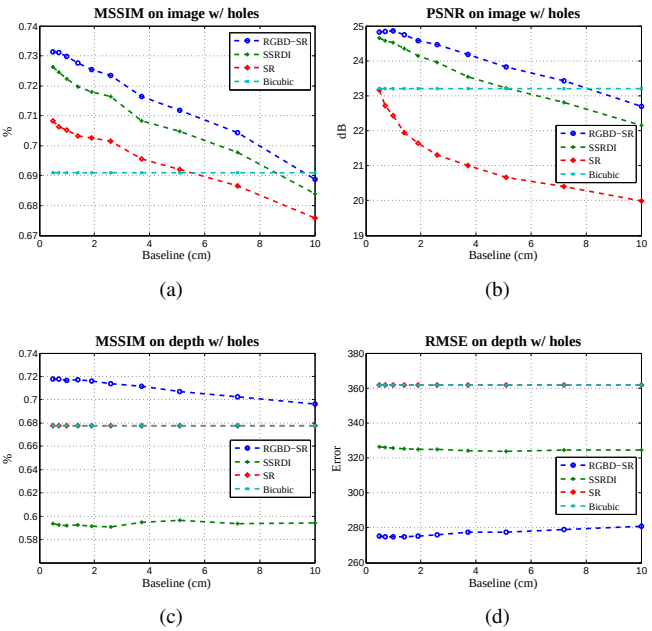

Figure 4. Analysis of the robustness of the methodologies for different baselines (distance of the virtual camera w.r.t. to the reference frame).

(a) Intensity image with RGBD-SR (b) Intensity image with SSRDI

(c) RGBD-SR (d) SSRDI (e) Bicubic

(f) RGBD-SR (g) SSRDI (h) Bicubic

(i) RGBD-SR (j) SSRDI (k) Bicubic

Figure 5. Images produced with the our method (RGBD-SR) and the SSRDI method. We can see that both methods produce better visual appearance when compared to the bicubic interpolation. However, the SSRDI method falls into local minimum in some areas as shown in Figures 5g and 5j .

Metric	RGBD-SR	SSRDI	SR	Bicubic
MSSIM	**0.933**	0.913	0.887	0.905
PSNR	**25.11**	24.46	23.97	23.55

Table I
COMPARISON BETWEEN THE KINECT SVGA IMAGE AND THE HR ESTIMATED FROM A SET OF LR KINECT VGA IMAGES.

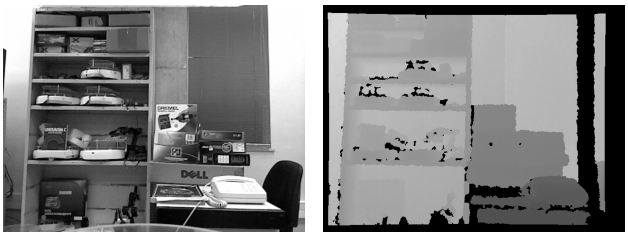

(a) Intensity Image (b) Depth Map

Figure 6. Image and depth maps with resolution 640×480 acquired with a Kinect in the laboratory.

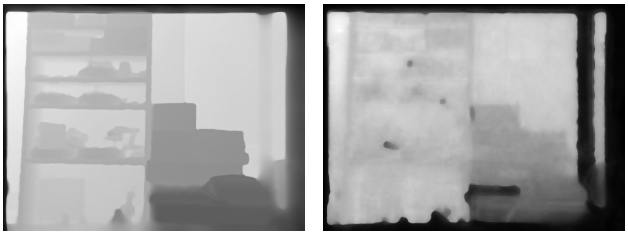

(a) Depth with RGBD-SR (b) Depth with SSRDI

Figure 7. Depth maps produced by the our methodology (RGBD-SR) and the SSRDI method.

method proposed by [16] for RGB-D image registration.

It can be seen in Figure 7 that the depth map produced by the SSRDI method falls into local minimum in some areas and the image reconstruction algorithm is greatly affected by the image noise in areas with low texture information. Since our method uses information from multiple depth maps, the chances that the image reconstruction process converge correctly increases, in addition it is possible to obtain a more robust and accurate result.

The comparison performed by using different metrics against other methods is shown in the Table I. The proposed method in this work (RGBD-SR) leads in performance, followed by SSRDI method which presented a better result than bicubic interpolation. The resulting images for RGBD-SR and SSRDI can be seen in Figure 5. We selected some key regions indicated by red rectangles and compared with the same regions of the groudtruth image (the result of the bicubic interpolation is also shown). It can be readily seen that our method produces the best results in all cases and that the SSRDI method produced some distortions in these areas mainly because the reconstruction optimization process fell into a local minimum.

V. CONCLUSION AND FUTURE WORK

In spite of the large number of works in super-resolution on imaging and depth maps, there are a few efforts which combine these two kinds of information to improve the final result. To fill this gap, in this work we propose a method capable of estimating simultaneously images and depth maps in higher resolution than that provided by the sensor. Since our method is based on a reconstruction approach, it is also able to estimate the depths not captured by the sensor.

Our experiments showed that, in several cases where there were failures, lost or deteriorated regions (e.g. holes) in the depth map, our methodology correctly estimated the depth information, and thanks to the fusion of image and depth map reconstruction, it was possible to improve the results for both images and the depth maps.

As future work we intend to adapt the reconstruction model to different luminance conditions and extend it to handle color information as discussed in [17].

REFERENCES

[1] M. Meilland and A. I. Comport, "Super-resolution 3D tracking and mapping," *Proc. ICRA*, pp. 5717–5723, May 2013.

[2] J. Sturm, N. Engelhard, F. Endres, W. Burgard, and D. Cremers, "A Benchmark for the Evaluation of RGB-D SLAM Systems," in *Proc. IROS*, Oct. 2012.

[3] J. Diebel and S. Thrun, "An application of markov random fields to range sensing," in *Advances in neural information processing systems*, 2005, pp. 291–298.

[4] Q. Yang, R. Yang, J. Davis, and D. Nistér, "Spatial-depth super resolution for range images," in *Proc. CVPR*. IEEE, 2007, pp. 1–8.

[5] U. Mudenagudi, A. Gupta, L. Goel, A. Kushal, P. Kalra, and S. Banerjee, "Super resolution of images of 3d scenecs," pp. 85–95, 2007.

[6] T. Tung, S. Nobuhara, and T. Matsuyama, "Simultaneous super-resolution and 3d video using graph-cuts," in *Proc. CVPR*. IEEE, 2008, pp. 1–8.

[7] B. Goldlücke and D. Cremers, "A superresolution framework for high-accuracy multiview reconstruction," in *Pattern Recognition*. Springer, 2009, pp. 342–351.

[8] A. V. Bhavsar and A. Rajagopalan, "Resolution enhancement in multi-image stereo," *IEEE Trans. PAMI*, vol. 32, no. 9, pp. 1721–1728, 2010.

[9] M. Unger, T. Pock, M. Werlberger, and H. Bischof, "A convex approach for variational super-resolution," in *Pattern Recognition*, 2010, pp. 313–322.

[10] H. S. Lee and K. M. Lee, "Simultaneous Super-Resolution of Depth and Images Using a Single Camera," *Proc. CVPR*, pp. 281–288, Jun. 2013.

[11] P. J. Huber, "Wiley series in probability and mathematics statistics," *Robust Statistics*, pp. 309–312, 1981.

[12] J. Stühmer, S. Gumhold, and D. Cremers, "Real-time dense geometry from a handheld camera," in *Pattern Recognition*, 2010, pp. 11–20.

[13] A. Chambolle and T. Pock, "A first-order primal-dual algorithm for convex problems with applications to imaging," *Journal of Mathematical Imaging and Vision*, vol. 40, no. 1, pp. 120–145, 2011.

[14] T. Pock and A. Chambolle, "Diagonal preconditioning for first order primal-dual algorithms in convex optimization," in *Proc. ICCV*. IEEE, 2011, pp. 1762–1769.

[15] D. Scharstein and R. Szeliski, "A taxonomy and evaluation of dense two-frame stereo correspondence algorithms," *International journal of computer vision*, vol. 47, no. 1-3, pp. 7–42, 2002.

[16] F. Steinbrucker, J. Sturm, and D. Cremers, "Real-time visual odometry from dense rgb-d images," in *Proc. ICCV*. IEEE, 2011, pp. 719–722.

[17] B. Goldluecke, E. Strekalovskiy, and D. Cremers, "The natural vectorial total variation which arises from geometric measure theory," *SIAM Journal on Imaging Sciences*, vol. 5, no. 2, pp. 537–563, 2012.